Nanostructured Materials and Interfaces for Advanced Ionic Electronic Conducting Oxides

Matias Acosta[1*], Federico Baiutti[2*], Albert Tarancón[2,3], and Judith L. MacManus-Driscoll[1]

[1] Department of Materials Science and Metallurgy, University of Cambridge, 27 Charles Babbage Road, Cambridge CB3 0FS, United Kingdom.

[2] Catalonia Institute for Energy Research (IREC), Department of Advanced Materials for Energy, 1 Jardins de les Dones de Negre, Barcelona 08930, Spain.

[3] ICREA, 23 Passeig Lluís Companys, Barcelona 08010, Spain.

*These authors contributed equally.

Abstract

Mixed ionic electronic conductors (MIEC) are pivotal materials in a number of electrochemical devices which are relevant for clean energy technologies and industrial chemical processes. In this report progress, we provide an overview of the recent strategies to tune surfaces and interfaces of MIEC fluorite and perovskite oxides for solid oxide fuel cells and micro-solid oxide fuel cells electrodes. Most of the works presented focus on salient strategies to improve the

oxygen reduction reaction (ORR) and the fuel oxidation reaction kinetics. We provide insights on the current understanding of heterointerfaces in epitaxial thin films and vertically aligned nanocomposites for ORR kinetics. A selection of oxide materials having potential for thin-film anode application is also presented. We further discuss recent salient results in grain boundary engineering and ex-solution as well as strain engineering and photoactivation for the development of advanced electrodes.

Introduction

Mixed ionic electronic conductor (MIEC) oxides are key materials for high performance solid oxide fuel cells (SOFC), micro-solid oxide fuel cells (micro-SOFC), sensors and gas separation membranes, among other electrochemical devices. These technologies are at the core of electrochemical energy conversion of hydrogen into electricity, generation of renewable gases in power-to-gas schemes, artificial photosynthesis or photoelectrochemical CO_2 reduction, to name a few.[1–5] In this progress report, we focus on providing an overview of the recent advances of surface and interface nanostructuring strategies that have resulted in excellent performing cathodes and anodes for SOFC and micro-SOFC. We stress, however, that similar strategies to the ones describe here can also be applied to improve MIEC materials for other applications too.

Electrical power sources such as SOFCs and micro-SOFCs are one of the most prominent energy conversion devices due to their high efficiency and absence of moving parts. These devices can run with a broad variety of hydrocarbon fuels and feature low or even zero pollutant emissions depending on the fuel employed, playing a potential major role in the future sustainable energy scenario. Moreover, micro-SOFCs represent a promising alternative to the current state-of-the-art Ni-metal hydride and Li-ion batteries due to a remarkably higher energy

density, which opens up their application in portable power electronics. Despite the unmatched features of SOFCs, some limitations arise from their high operating temperatures, typically above 750 °C. Hence, there is an interest to reduce their operational temperature, especially if such devices are planned to be integrated in consumer electronics in the form of micro-SOFCs. At low temperatures, however, the polarization losses at the electrodes become critical and reduce the SOFC performance substantially.[6,7]

Efficient electrodes should have large catalytic activity, good chemically stability, large oxygen ionic and electronic transport, and engineered microstructures to favour gas diffusion. Recent reviews provided excellent guidelines on state-of-the art tailored microstructures for electrodes[8] and on strategies to produce them.[9] Typically, the oxygen reduction reaction (ORR) at the cathode is the bottleneck for the reduction of the operation temperature in hydrogen-fuelled SOFCs due to the sluggish kinetics of oxygen exchange at reduced temperature.[7] In the particular case of micro-SOFCs, the anode could also be a limiting factor since the fabrication of cermets in thin film form is not well established yet.

The present progress report focuses on the development of highly performing nanostructured oxides and interfaces for SOFC and micro-SOFC for both cathode and anode electrodes. We provide an emphasis on thin film electrode materials suitable for micro-SOFCs thereby providing insights into ORR and oxidation process mechanisms at the nanoscale. We initially present state-of-the-art strategies to nanostructure the surface of perovskite cathodes to improve ORR kinetics. This topic has been recently treated elsewhere but mostly with a focus on degradation mechanisms[10,11] or porous materials[12], whereas here it will be discussed on the basis of the key role of the surface to improve the ORR intrinsically, *i.e.* skipping here the effect of the porosity. This is followed by introducing heterointerfaces and the current understanding of their role on improving oxygen transport and ORR kinetics. Thereafter, we provide insights into the

state-of-the-art of nanostructured anode materials. We focus this section on the latest results on ceria and acceptor-doped perovskites as well as on their potential as thin-film anodes. In addition, we also provide a literature review into two strategies that recently paved the way of development of remarkable cathodes and anodes such as grain boundary engineering and ex-solution. Lastly, we briefly discuss the concepts of strain engineering and photoactivation for the development of advanced electrodes.

1. Nanostructuring Cathodes and Interfaces to Improve Oxygen Reduction Kinetics

Several possible reaction steps have been identified in relation to oxygen exchange reactions, as schematically illustrated in figure 1. Although a comprehensive picture is still lacking, and different interpretations are given with respect to the identification of the limiting steps,[13,14] it is commonly accepted that an important role in achieving fast oxygen exchange is bulk transport kinetics. This is because the reacting species involved in the exchange process (electrons and oxygen vacancies) should reach the reactive sites for the ORR to occur. The reactive sites in cathodes are generally those at the triple phase boundary where electrolyte, electrode, and gas phases are in contact and provide the required reactive species. In MIEC, however, the sites are extended to a large portion of the electrode surface due to the mixed ionic-electronic conductivity (figure 1). De Souza and Kilner[15] pointed out that an empirical correlation exists between oxygen diffusivity and the surface exchange coefficient. Hence, the search for highly performing electrode materials should include the optimization of bulk chemistry in terms of supply of oxygen vacancies and electronic charges.

The modification of surface chemistry is key for reactivity enhancement. Hence, strategies for tuning the availability of surface oxygen vacant sites or for altering the surface electronic state is of uttermost importance. Such local effects, which are typically confined in nanometer length

scales, i.e., nanoionics, are of particular relevance in the case of thin film materials owing to the high interface density, the low thickness involved, and the possibility of obtaining fully packed vertically aligned columnar grains.[16]

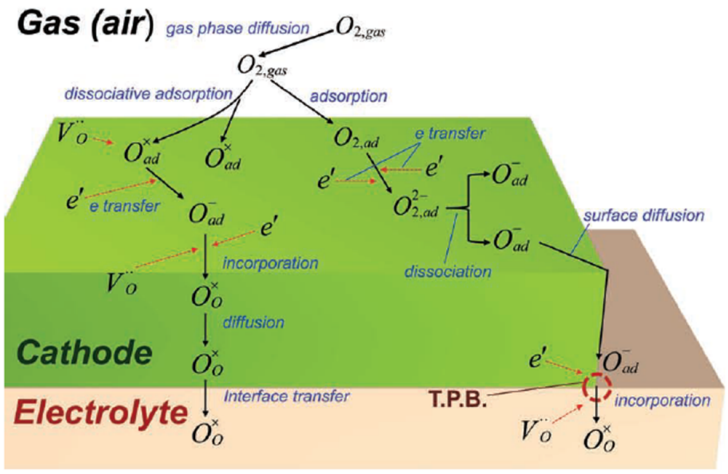

Figure 1: Schematic illustration of possible elementary reaction steps during cathode reactions. Copyright 2011 Wiley. Used with permission from Jung and Tuller, A New Model Describing Solid Oxide Fuel Cell Cathode Kinetics: Model Thin Film $SrTi_{1-x}Fe_xO_{3-\delta}$ Mixed Conducting Oxides–a Case Study, Advanced Energy Materials.[17]

1.1. Coating Cathodes' Surfaces

The highest efficiency loss of a SOFC operating at reduced temperature generally come from the polarization resistance associated with the ORR at the cathode. This is due to the complex intermediate steps of this reaction and their slow kinetics. Hence, developing advanced cathodes via surface engineering is of paramount importance.[7] The nanostructure, chemistry, and crystal structure of cathode surfaces plays a decisive role in the ORR.[10,18–20]

Cathode surfaces have been tuned with oxides and noble metals. Noble metals like Pt have generally been used due to their high catalytic activity for ORR. However, their cost and

long-term reliability can limit their technological implementation. Surface coatings with oxides offer great versatility and reduced costs. Indeed, coating the surface of cathodes with oxides can improve commercial SOFC performance and long term stability.[21]

Below, we provide details of some of the most salient recent examples of materials' nanostructuring approaches. Although we focus most of the results in this manuscript to crystalline materials, it is worth highlighting that surface decoration/precipitation of amorphous phases also appears to be a promising and yet to be explored avenue to improve ORR kinetics.[22,23]

Chen et al.[24] developed a multi-phase 30-nm thick catalyst coating capable of improving considerably the ORR kinetics of both porous and dense (La,Sr)(Co,Fe)O_3 (LSCF) cathodes. The catalyst consisted of a $PrBa_{0.8}Ca_{0.2}Co_2O_{5+d}$ conformal thin film coating and nanoparticles of $BaCoO_{3-x}$ and $PrCoO_{3-x}$. It was produced by a solution infiltration process of the cathode and firing at 800 °C for 1 h. The performance of the LSCF and catalyst-coated LSCF cathode were evaluated by electrochemical impedance spectroscopy (EIS) and electrical relaxation experiments. An oxygen exchange coefficient $k_q = 2.39 \times 10^{-3}$ cm s^{-1} and an activation energy of 0.91 eV was found for the catalyst-coated LSCF at 600 °C in air. The activation energy of the untreated LSCF was 1.46 eV and the k_q was more than one order of magnitude higher than that of the catalyst-coated LSCF. Moreover, at the same conditions, the catalyst-coated LSCF featured an area specific resistance (ASR), ASR= 0.312 Ω cm^2, which was approximately 8-times lower than that of LSCF under the same measuring conditions. Importantly, the SOFC containing the catalyst-coated LSCF showed much more stable operation within 250 h of testing. Using the distribution of relaxation times of the impedance data and density functional theory calculations, the authors proposed that the catalyst enhances the ORR and transport too. Initially, a rapid oxygen adsorption and dissociation takes place on the $BaCoO_{3-x}$ and $PrCoO_{3-x}$

nanoparticles due to the presence of a large number of oxygen vacancies. Thereafter, the dissociated oxygen species are transported through the $PrBa_{0.8}Ca_{0.2}Co_2O_{5+d}$ into LSCF. The increased stability of the catalyst-coated LSCF was associated with a suppression of Sr^{2+} surface segregation.[24]

Segregation of dopants (mostly Sr^{2+}) towards the surface of perovskite cathodes and concomitant precipitation of (Sr^{2+}-rich) dielectric phases is one of the most critical degradation mechanisms of cathodes. It determines the ORR kinetics to a great extent and can even override the activity of different crystallographic orientations.[10] The degradation process has been reviewed thoroughly elsewhere.[10,11] Here we provide details only of some key recent works that indicated strategies to mitigate this issue by producing nanostructured materials. Wen et al.[25] investigated in detail the Sr^{2+} surface segregation in epitaxial $(La_{1-x}Sr_x)CoO_3$ (LSC_{113}) by using time- and temperature-dependent in situ synchrotron-based ambient pressure X-ray photoelectron spectroscopy (XPS). They found that the onset of Sr^{2+} surface segregation occurs at 350 °C and its surface content increases quite considerably up to 520 °C. Moreover, they also observed that the activation energy for the thermally activated process of Sr^{2+} diffusion is E_a=1.04 eV, which is considerably lower than the activation energy for Sr^{2+} segregation in $SrTiO_3$ (E_a=3.85 eV). This was attributed to the high concentration of surface oxygen vacancies in the surface of LSC_{113}. The surface oxygen exchange coefficient k_q =1 x 10^{-8} cm s^{-1} of the as-grown LSC_{113} as a function of time is shown in figure 2. The gradual degradation of k_q as a function of time is a result of the Sr^{2+} surface enrichment.[25]

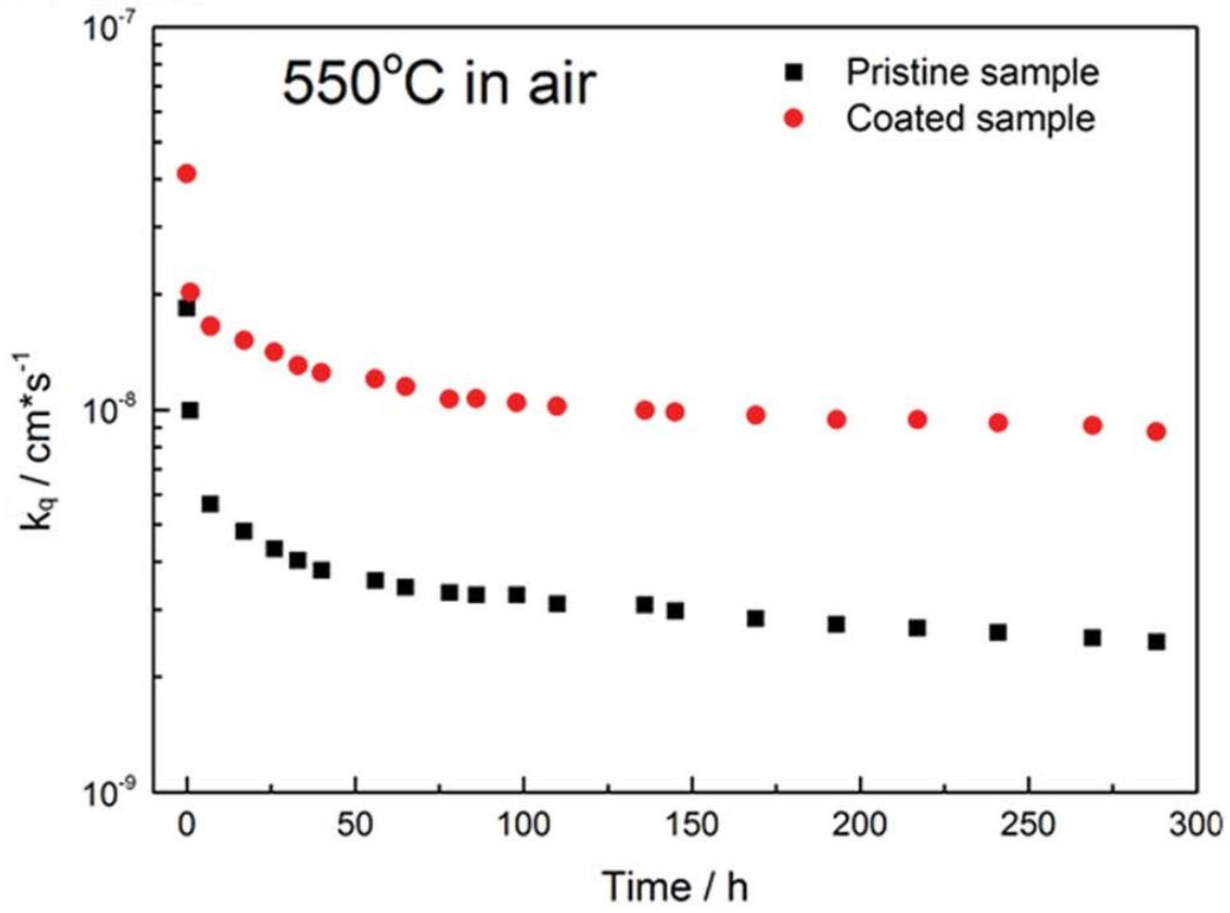

Figure 2: Surface oxygen exchange coefficient k_q as a function of time for LSC_{113} and ZrO_2 coated LSC_{113}. The EIS measurements were conducted at 550 °C in ambient air. Reproduced with permission from ref.[25] Copyright 2018, The Royal Society of Chemistry.

Suppression of Sr^{2+} surface segregation can be achieved by surface chemical modifications. Wen et al.[25] used ALD to produce a thin film surface coating of ZrO_2 on LSC_{113}. They observed that the coating modified only the surface chemistry and not the strain state. Sr^{2+} surface species, as measured by XPS, were considerably reduced in the ZrO_2 coated LSC_{113} as compared to the untreated sample. As shown in figure 2, the ZrO_2 coated LSC_{113} features an improved exchange kinetics performance over the 300 h tested.

Tsvetkov et al.[19] provided further insights on the improvement of ORR kinetics by surface chemical modifications on LSC_{113}. Using metal chloride solutions, they coated LSC_{113} with sub-monolayers of different cations whose binary oxides have lower (V^{5+}) or higher (Nb^{5+}, Ti^{4+}, Zr^{4+}, Hf^{4+}, or Al^{3+}) enthalpies for the formation of oxygen vacancies as compared to the vacancy formation enthalpy in LSC_{113}. Figure 3a shows the oxygen exchange coefficient k_q as a function of time for the untreated and surface coated materials. The materials have k_q values that vary quite considerably between 10^{-9} cm s^{-1} and 10^{-7} cm s^{-1}. Moreover, they feature different stability over time. Using XPS, the authors demonstrated that the strongest degradation in properties occurs in the samples with higher Sr^{2+} surface segregation. The Hf-coated material feature the best performance with an almost constant k_q= 3 x 10^{-8} cm s^{-1} over the 30 h tested.

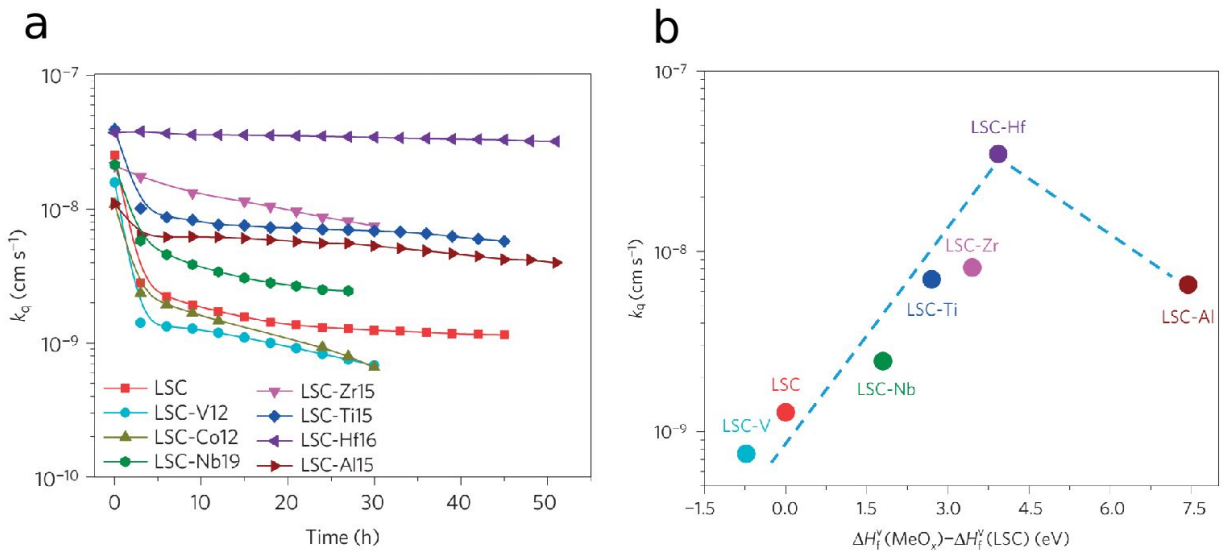

Figure 3: a) Surface exchange coefficient k_q obtained from electrochemical impedance spectroscopy as a function of time on uncoated LSC_{113} (LSC) and coated LSC_{113} with V_2O_5 (LSC-V), Nb_2O_5 (LSC-Nb), TiO_2 (LSC-Ti), ZrO_2 (LSC-Zr), HfO_2 (LSC-Hf), and Al_2O_3 (LSC-Al). Measurements were done at 530 °C in air. b) Surface exchange coefficient k_q as a function of

the enthalpy difference of the oxygen vacancy formation energy and that of LSC_{113}. The y-axis shows k_q measured in air at 550 °C after 27 h of testing. Reproduced with permission from ref.[19] Copyright 2016, Nature Publishing Group.

Using X-ray absorption spectra, Tsvetkov et al.[19] demonstrated that less reducible cations (Nb^{5+}, Ti^{4+}, Zr^{4+}, Hf^{4+}, and Al^{3+}) in the form of surface oxide layers decrease the content of surface oxygen vacancies, in turn leading to a higher oxidation state of Co in LSC_{113}. This suppresses the electrostatic attraction of Sr^{2+} towards the La^{3+} sites and the precipitation of Sr^{2+}-rich dielectric phases at the surface. The authors found a volcano-like dependence in the oxygen exchange coefficient, k_q, when plotted as a function on the difference between the enthalpy of oxygen vacancy formation of the binary oxides and LSC_{113} (figure 3b). This challenges the notion that a high oxygen vacancy concentration facilitates oxygen exchange kinetics in transition metal oxides. An excessive content of oxygen vacancies at the surface will slow down the ORR kinetics due to an enhanced Sr^{2+} surface segregation. The optimum kinetics are achieved when the surface oxygen vacancy concentration provides a gain in ORR kinetics but still allows certain chemical surface stability to minimize the precipitation of Sr^{2+}-rich dielectric phases.[19]

Li et al.[26] synthesized LSC_{113} thin films using pulsed laser deposition (PLD) and decorated the films by exposing them to $Sr(NO_3)_2$ or $Co(NO_3)_3$ aqueous solutions. Compared to the untreated LSC_{113}, $Sr(NO_3)_2$ decoration increased the content of Sr^{2+} on the surface. In contrast, decoration with $Co(NO_3)_3$ decreased the content of Sr^{2+} on the surface and enhanced Co concentration. Electrochemical impedance spectroscopy (EIS) of the samples with different Sr^{2+} surface content was done at 600 °C in air. The oxygen exchange coefficients, k_q, obtained from these measurements are displayed in figure 4.

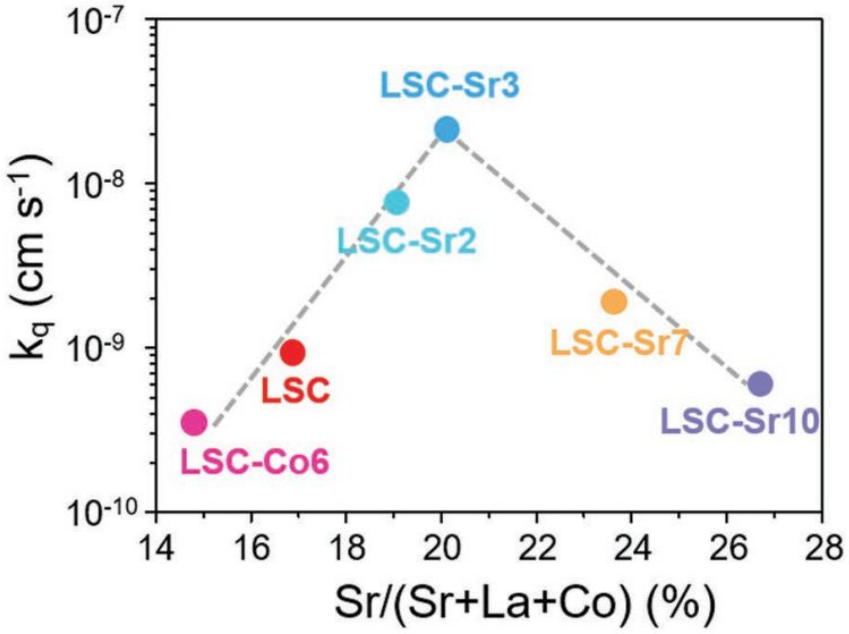

Figure 4: Surface oxygen exchange coefficient k_q as a function of surface Sr^{2+} content. LSC-Srx or LSC-Cox represents the molar surface excess of Sr and Co as measured by XPS, respectively. Reproduced with permission from ref.[26] Copyright 2018, Wiley.

Figure 4 shows that k_q and surface Sr^{2+} content are related by a volcano-type relationship, similarly as shown in figure 3 for different oxide coatings. This indicates that an optimum SrO surface concentration enhances the ORR kinetics. The results of time-of-flight secondary ion mass spectrometry (ToF-SIMS) revealed that the 3 at. % SrO coated LSC_{113} features the largest oxygen exchange activity. To investigate the mechanism of enhancement of the ORR kinetics, the authors annealed samples with different Sr^{2+} surface content at 600 °C in air for 12 h and investigated the surface with scanning electron microscopy (SEM) and Auger electron spectroscopy (AES) mapping. They found that the 3 at. % SrO coated LSC_{113} has a rather homogeneous segregation with no presence of Sr^{2+}-rich precipitates. Hence, they proposed that the highly mobile Sr^{2+} in solution during the decoration process migrates preferentially towards

specific surface sites (e.g. grain boundaries or dislocations) effectively suppressing excessive Sr^{2+} segregation.

Using plane wave density functional theory (DFT) calculations, Li et al.[26] demonstrated that Sr^{2+} migrates preferentially towards Co-terminated surface sites. However, if these sites are covered with Sr^{2+} (arising from the decoration process), the migration of Sr^{2+} towards the surface becomes energetically unfavourable. Interestingly, the authors also found that excess surface Sr^{2+} from the decoration process forms A-site deficient polycrystalline perovskite-like precipitates in-situ at the probing temperatures. They proposed that these precipitates are responsible of the enhanced electrochemical activity of the decorated LSC_{113}. The results are in agreement with those of Tsvetkov et al.[4] In contrast to the findings of these works, decoration of LSC_{113} with SrO deposited using PLD led to a reduced oxygen exchange activity.[20] Li et al.[26] attributed these discrepancies to the preferential Sr^{2+} coating at the surface in specific sites (e.g. grain boundaries or dislocations) owing to the solution-based method employed. In contrast, PLD forms a continuous surface layer of SrO and is performed at much higher temperature.[26]

Crumlin et al.[27] demonstrated that coating LSC_{113} with $(La_{1-x}Sr_x)_2CoO_4$ (LSC_{214}) is a successful strategy to improve the ORR kinetics. Using PLD, the authors decorated the surface of LSC_{113} with LSC_{214} thin films of thicknesses between 0.1 nm and 15 nm. The complete set of LSC_{214}-decorated films feature enhanced k_q values compared to the untreated films. The films with thinner coating led to surface nanoislands instead of a continuous coverage. Using EIS, the authors found that the samples with nanoisland coverage had the highest surface oxygen exchange coefficients with $k_q \sim 1 \times 10^{-6}$ cm s^{-1} at 550 °C and 1 atm O_2. This indicated an enhancement on ORR kinetics of ~3-4 orders of magnitude as compared to bulk LSC_{113}. The enhancement was attributed to the large number of heterointerfaces between LSC_{113} and LSC_{214}.[27] Using a similar approach, Hong et al.[28] demonstrated that coating $La_{0.8}Sr_{0.2}FeO_{3-\delta}$

with $(La,Sr)_2FeO_{4-\delta}$ results in an enhancement of the ORR kinetics by one order of magnitude as compared to the kinetics in untreated $La_{0.8}Sr_{0.2}FeO_{3-\delta}$.

1.2. Epitaxial Superlattices and Vertically Aligned Nanocomposites for Cathodes

In the present section, the mechanisms of enhancement of ORR kinetics at different perovskites and Ruddlesden-Popper phases by using heterostructures are described in detail. Heterostructured systems are typically studied in the form of epitaxial superlattices (figure 5a) or vertically aligned nanocomposites (VAN, figure 5b). The high interface density makes them quite attractive to investigate fundamental phenomena.

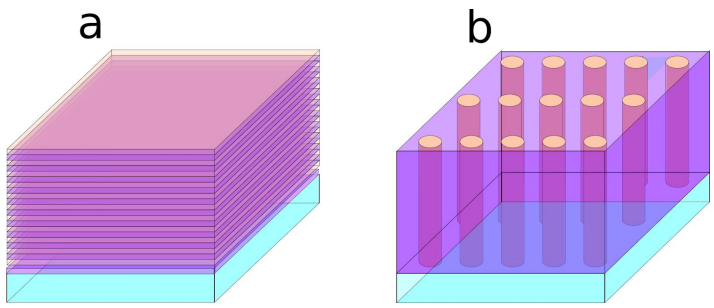

Figure 5: Schematic representation of a) epitaxial superlattice and b) VAN.

Epitaxial superlattices are complex structures that require a sequence of depositions of the two materials being investigated. On the other hand, VAN are thermodynamically stable thin films composed of two single crystalline phases: matrix and nanopillars. They can be easily obtained by self-assembly and feature interfaces perpendicular to the substrate that are highly beneficial for probing properties and for device integration owing to the out-of-plane geometry. VAN have a very large interfacial area which favours phase interaction and high crystallinity throughout micrometer range thickness. This makes it possible to obtain high quality dense and coherent

VANs with remarkable properties. The development of VANs offers a tremendous opportunity to improve exchange kinetics due to the increased triple phase boundary density (TPB).[29–31] Several heterointerfaces feature a large ionic and/or electronic conductivity.[29,32] Heterointerfaces between perovskites and the Ruddlesden-Popper phases have been thoroughly investigated in recent years as cathodes and functional interlayers between electrolyte and cathode.[33,34] Some remarkable examples include LSC_{113}/LSC_{214}, $Nd_{0.5}Sr_{0.5}CoO_{3-\delta}/Nd_{0.8}Sr_{1.2}CoO_{4\pm\delta}$, and $Sm_{0.2}Ce_{0.8}O_{2-\delta}$ /$Sm_{0.5}Sr_{0.5}CoO_{3-\delta}$.[33,35–38]

Sase et al.[35–37] reported for the first time the remarkable enhancement of oxygen exchange kinetics of ~3-4 orders of magnitude in LSC_{113}/LSC_{214} heterointerfaces as compared to the separate phases. Recently, many works focused on designing controlled heterointerfaces and VAN to investigate the mechanisms behind this enhancement. Stämmler et al.[39–41] investigated the synthesis and oxygen exchange kinetics of VAN based on LSC_{113} and LSC_{214}. They managed to vary the relative content of LSC_{113} and LSC_{214} phases considerably by changing the composition of the targets used for PLD deposition. The VAN nanopillars featured a typical lateral size between 20 nm and 100 nm, which is smaller than those found in other VAN in the same system.[42] The analysis of the resulting phases indicated that some VAN consisted of LSC_{113} and LSC_{214}, whereas others featured non-equilibrium structures like $La_{0.7}Sr_{0.3}Co_{0.9}O_{3-\delta}$ and $(La,Sr)_{n+1}Co_nO_m$ (N>1). The $La_{0.7}Sr_{0.3}Co_{0.9}O_{3-\delta}$ phase is not stable in bulk materials, whereas the $(La,Sr)_{n+1}Co_nO_m$ phase is thermodynamically stable only with much higher Sr^{2+} content. The resulting phases in the different VAN films depended only on target composition since all deposition conditions were kept constant.

Figure 6 shows the nanostructure of VAN (labelled as “SATP” and “post-crystallized amorphous film”) as well as single phase thin films of LSC_{113} (labelled “Co-deficient P”) and of LSC_{214} (labelled “higher order R”). The formation of metastable phases in VAN was attributed to

inhibited homogeneity owing to low cation mobility or low density of crystal nuclei during PLD deposition. Figure 6 also shows the dependence of oxygen exchange coefficients k_q of LSC_{113}, LSC_{214}, and VAN comprised of those phases, $La_{0.7}Sr_{0.3}Co_{0.9}O_{3-\delta}$, and $(La,Sr)_{n+1}Co_nO_m$ (N>1). The oxygen exchange coefficients k_q are presented as a function of the thin films nominal LSC_{214} phase fraction (color code in figure caption indicates the materials' phase content). The coefficients were obtained by EIS at 600 °C and 1 bar O_2 partial pressure. The calculated dashed purple reference curve k_{ideal} corresponds to a two-phase material with absence of TPB effects.

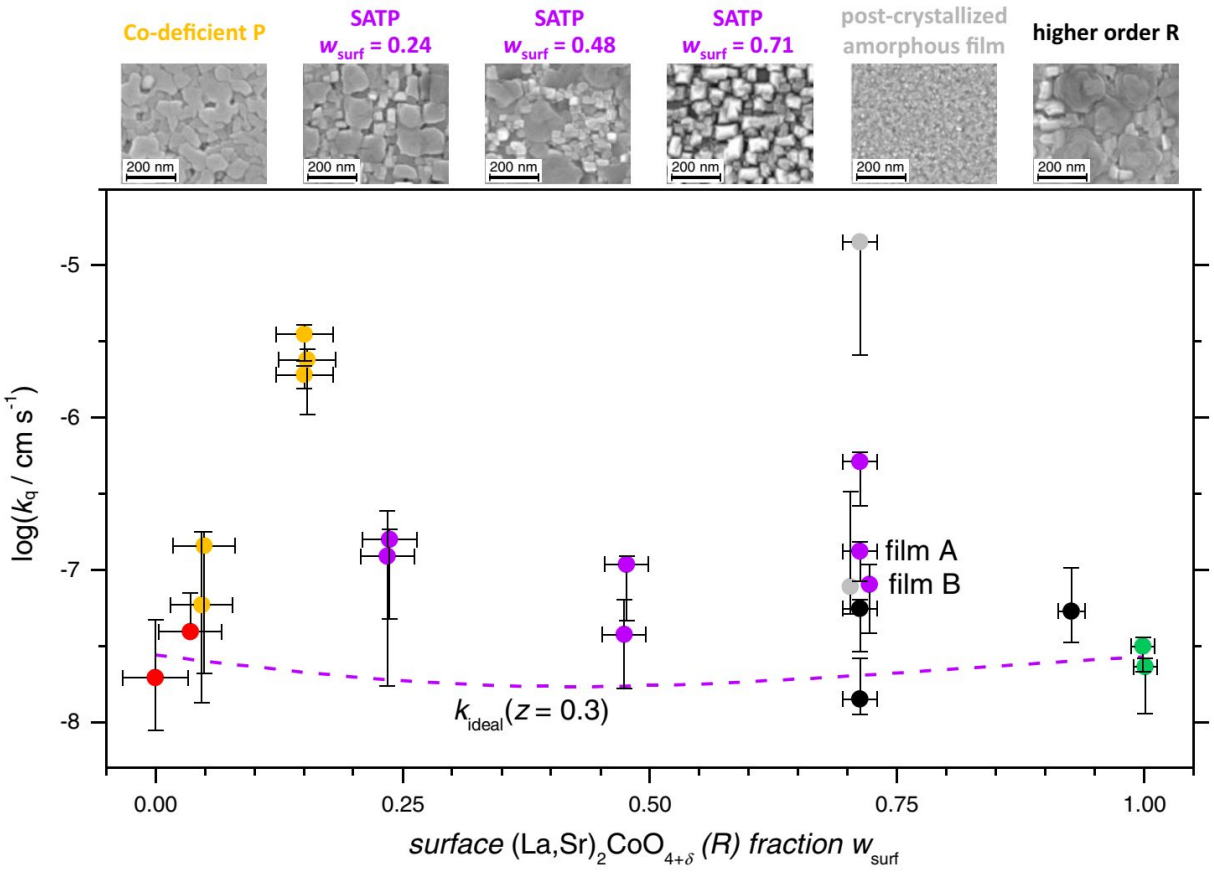

Figure 6: ORR oxygen exchange coefficients k_q of LSC_{113}, LSC_{214} and VAN comprised of these phases, $La_{0.7}Sr_{0.3}Co_{0.9}O_{3-\delta}$, and $(La,Sr)_{n+1}Co_nO_m$ (N>1) as function of their nominal LSC_{214} phase

fraction, calculated from EIS. The oxygen exchange coefficients k_q were measured at 600 °C and 1 bar O_2 partial pressure. The dashed purple curve indicates the reference activity k_{ideal} of a two-phase material with absence of TPB effects. Color indicates the phases; red: LSC_{113}, orange: Co-deficient LSC_{113} ($La_{0.7}Sr_{0.3}Co_{0.9}O_{3-\delta}$), purple: VAN composed of LSC_{113} and LSC_{214}, grey: VAN with presence of amorphous phase, black: VAN with presence of higher-order LSC_{214} phase ($(La,Sr)_{n+1}Co_nO_m$ (N>1)), green: LSC_{214}. Reproduced with permission of ref.[39] Copyright 2017, The Electrochemical Society.

Most VAN comprising LSC_{113} and LSC_{214} feature a higher activity compared to the ideal material without presence of TPB effects. Hence, the heterointerfaces; *i.e.* TPBs, are responsible for the ORR kinetics enhancement. The approximate specific k_q of the TPB is in the range of 2-9 · 10^{-13} cm^2/s at 600 °C and at 1 bar O_2. VAN with the presence of $(La,Sr)_{n+1}Co_nO_m$ (N>1) feature a strong scattering and low ORR kinetics. This was attributed to the inhibition of the effect of the TPB between LSC_{113} and LSC_{214} owing to the parasitic phase. The authors speculated that the post-crystallized amorphous VAN exhibits the highest activity due to their large TPB density. Interestingly, Sari et al.[43] also observed a considerably high activity and low specific resistance for co-sputtered amorphous films obtained using LSC_{113} and LSC_{214} targets. None of the works discussed in detail the role of amorphous heterointerfaces or even possibly the role of amorphous/crystalline heterointerfaces on the oxygen exchange kinetics.

Ma et al.[42] investigated the mechanism of oxygen exchange kinetics in LSC_{113}/LSC_{214} VAN grown using PLD. They revealed that LSC_{113} within VAN films features an energy band gap of 1.5 eV at room temperature that evolves to a metallic-like behavior with no energy band gap at and above 250 °C. The semiconductor-metallic transition at the surface is reversible upon cooling and was ascribed to the creation of oxygen vacancy energy levels in the band gap

similarly as in the single-phase LSC_{113}. In contrast, the conductivity of LSC_{214} in VAN and as a single phase thin film changes considerably. The surface of LSC_{214} within VAN becomes metallic-like above 250 °C, whereas as a single phase it features an energy band gap of 1.0 eV at this temperature. This was attributed to the facile reduction of the LSC_{113} surface, which raises the electron chemical potential (Fermi level) and decreases the chemical potential of oxygen in the LSC_{214}. In agreement with these results, it was also shown that at 250 °C, Co features a greater reducibility in LSC_{214} within a superlattice structure of LSC_{113}/LSC_{214} as compared to that of Co in a LSC_{214} single-phase thin film.[44] These observations indicate that the heterointerface promotes the oxygen migration from the LSC_{214} into LSC_{113} and electrons from LSC_{113} to LSC_{214}. The exchange of oxygen vacancies and injection of electrons across the heterointerface raises the Fermi level of LSC_{214} and enables long-range charge neutrality. This anionic and electronic charge transfer is responsible of the disappearance of the energy gap of LSC_{214} within VAN above 250 °C. Concomitantly, a larger concentration of free electrons becomes available in the p-type LSC_{214} which enhances the oxygen reduction kinetics. Another important aspect is that VAN had a less pronounced surface Sr^{2+} enrichment at temperatures up to 400 °C as compared to single phase thin films. This led to more stable oxygen exchange kinetics.[42] The chemical stability of LSC_{113} was also improved in other heterostructures.[32] Nonetheless, the thermal energy above 450 °C was sufficient to promote Sr^{2+} surface enrichment and precipitation of phases in both VAN and LSC_{113} thin films. This resulted in a strong degradation of the oxygen exchange kinetics.[42,45]

It has also been proposed that the Sr^{2+} concentration at the heterointerface between LSC_{113} and LSC_{214} is the key factor determining the enhancement of its oxygen exchange kinetics. Coherent Bragg rod analysis, XPS, and ToF-SIMS revealed a large concentration of Sr^{2+} under operando conditions at the heterointerface of LSC_{113}/LSC_{214}.[46,47] Theoretical calculations demonstrated

that there is an energy gain of 0.8-1.5 eV when Sr^{2+} replaces La^{3+} at the LSC_{214} surface and interfaces.[47–49] The Sr^{2+} segregation from the perovskite towards the LSC_{113}/LSC_{214} interface lifted the oxygen 2p band center relative to the Fermi level and increased the oxygen surface exchange kinetics.[47,50] In agreement with these theoretical results, differential coherent Bragg rod analysis at the LSC_{113}/LSC_{214} heterointerface indicated that the oxygen 2p band center relative to the Fermi level becomes comparable to other perovskites like $Ba_{1-x}Sr_xCo_{1-y}Fe_yO_{3-\delta}$, which typically feature considerably high oxygen surface exchange kinetics.[47] It is worth highlighting that the Sr^{2+} enrichment at heterointerfaces had been described as a different phenomenon from the detrimental precipitation of dielectric Sr^{2+}-rich phases that generally reduce ORR.[47,51]

Chen et al.[45] recently developed trilayers of $LSC_{113}/LSC_{214}/LSC_{113}$ and $LSC_{113}/La_2NiO_{4+\delta}/LSC_{113}$. They demonstrated that the level of oxygen stoichiometry at heterointerfaces and their reducibility depends on the type of neighboring oxide (i.e., heterointerface electrostatic potentials). An electrostatic potential as low as 0.1 eV near the interface can introduce a considerable difference in the oxygen nonstoichiometry in LSC_{113} and at the heterointerface. Interestingly, this approach can result in heterointerfaces that are more or less easily reducible than single phase thin films. For instance, LSC_{113} and LSC_{214} are less reducible than the LSC_{113}/LSC_{214} heterointerface.[44,45] However, $Nd_2NiO_{4+\delta}$ is more reducible than the $Nd_2NiO_{4+\delta}/LSC_{113}$ heterointerface.[52] This might shed light on a correlation with the oxygen exchange kinetics. The heterointerface of LSC_{113}/LSC_{214} has faster kinetics for oxygen exchange than the single phases, whereas $Nd_2NiO_{4+\delta}$ has faster kinetics than the $Nd_2NiO_{4+\delta}/LSC_{113}$ heterointerface.[44,45,52] The heterointerface between LSC_{113} and $Ce_{0.90}Gd_{0.1}0O_{2-\delta}$ also appears to increase the oxygen exchange kinetics as compared to LSC_{113}. It was proposed that the kinetic enhancement is most likely related to reduced Ce^{4+} at the

heterointerface and a concomitant high density of oxygen vacancies.[53] The transport along heterointerfaces in this system is dominated by electronic conduction with semi-conductive behaviour at low temperatures and metallic-like behavior for temperatures above 400 °C.[32] Interestingly, it was proposed that the conductivity mechanism depends on the thickness and the number of bilayers in the superlattice.[32,53] Hence, it might be possible to tune oxygen reduction kinetics by altering the the thickness and the number of bilayers of the superlattice.

Chen et al.[45] also highlighted that the model explaining the the oxygen surface exchange kinetics thanks to preferential Sr^{2+} segregation along heterointerfaces cannot explain the lower content of oxygen vacancies in LSC_{113} within $LSC_{113}/LSC_{214}/LSC_{113}$ trilayers as compared to the content found in the single phase LSC_{113}. Moreover, upon annealing at 500 °C, they observed an increased content of reduced Co^{2+} in LSC_{113}. It was mentioned that if the temperature would result in an enrichment of Sr^{2+} on the La-site, then a more oxidized Co state would be expected in LSC_{113}.[45] Interestingly, Zheng et al.[38] found both an enrichment of Sr^{2+} content and reduced Co at the heterointerfaces of the perovskite $Nd_{0.5}Sr_{0.5}CoO_{3-\delta}$ and Ruddlesen-Popper $Nd_{0.8}Sr_{1.2}CoO_{4\pm\delta}$ superlattice grown by PLD. Using EIS, the authors showed that this system featured an oxygen surface exchange coefficient $k_q = 2.92 \times 10^{-07}$ cm s^{-1} at 10 % oxygen partial pressure and 500 °C. The oxygen exchange kinetics were ~2-3 orders of magnitude larger than those found in the individual phases. Zheng et al.[38] proposed that the higher concentration of oxygen vacancies at the heterointerface is the main reason for the enhanced oxygen exchange kinetics of the superlattice.

2. Anodes

The anodic reaction of oxidation in a SOFC can be written, in the exemplary case of hydrogen fuel, as:

$$H_2 + O_O^x \rightarrow H_2O + V_O^{\bullet\bullet} + 2e^/ \qquad \text{equation 1}$$

Unlike cathodes materials, the fundamental steps of fuel oxidation still remain poorly understood. As a rule of thumb, anodic materials should present not only high ionic and electronic conductivity and a high catalytic activity, but also the ability to withstand severe reducing conditions at high temperatures. The latter represents a strong limitation in the possible materials' selection, especially within the oxide families. For example, it hinders the use of most of the typical perovskite MIEC materials for cathodes such as cobaltites, manganites, and ferrites, which are prone to fast decomposition under low pO_2 and high T (figure 7).[54,55]

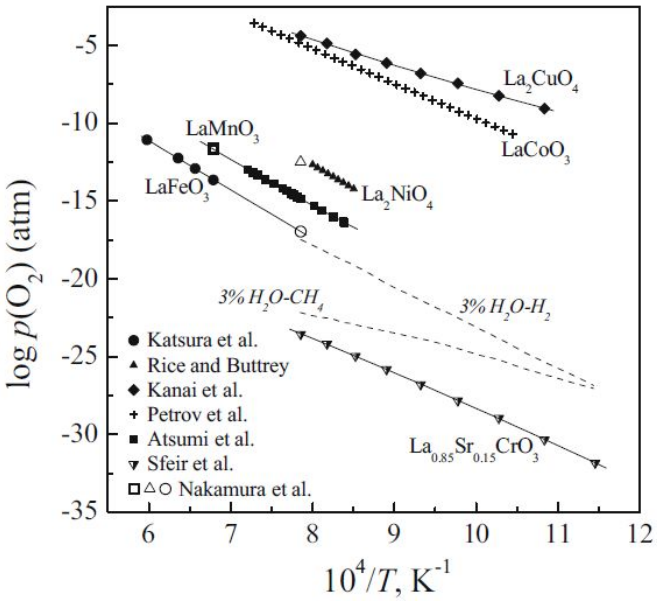

Figure 7. Comparison of the low pO_2 stability boundaries of common perovskites for electrode applications. The 3 % H_2O/H_2 and 3 % H_2O-CH_4 equilibrium lines are reported as a reference. One can observe that a stability region in typical anodic conditions exists only in the case of Cr-based perovskites. Reproduced with permission from ref.[54] Copyright 2008, Springer.

Owing to such strong limitation, classical anodic structures are composed by a porous catalytic metal (among which Ni has been identified as the most active and cost-effective[56]), or by metal-electrolyte composites (cermets), in such a way that the fuel oxidation is typically confined at the TPB.[2] Despite their high catalytic activity and good stability under reducing conditions, metal-based structures are strongly affected by structural instability (Ostwald ripening phenomena) and by low tolerance towards S poisoning (which becomes relevant in applications in which hydrocarbon fuels are used).[57] Moreover, although several methods are readily available for the preparation of thick layers of metal-YSZ composites starting from simple mixing in cermets to impregnation of ceramic backbones; the fabrication of nm-thick layers suitable for use in microdevices imposes severe constraints in using such classical approaches in microdevices.[58]

In the search of novel anodic compositions with enhanced performance and which possess compatibility with thin film technology, a promising route is represented by the exploration of functional oxides and heterostructures. This is because they are able to offer superior mechanical stability, a good catalytic activity and additional degrees of freedom for compositional and microstructural engineering at the nanoscale. Importantly, they also afford the extension of the reactive area far from the TPB, which is a strategy for decreasing the anode resistance.

Unlike cathodic materials, the search of thin film ceramic anodes is still at its infancy: noble metal layers are, by far, still the most employed materials for technological applications (e.g. micro-SOFC – a comprehensive summary can be found in ref.[59]). This opens up intriguing opportunities for new investigations. In the following paragraph, we give an account of selected oxide materials and structures that could find potential compatibility with thin film anodes technology.

2.1. Cerium Oxide

Acceptor doped cerium oxide, in which charge compensation for dopant incorporation occurs via the formation of oxygen vacancies, is widely employed as an electrolyte material for oxygen ionic conduction. However, under reducing conditions, the material is able to release additional oxygen from the lattice and to accommodate a large amount of oxygen hypostoichiometry, which is compensated by Ce reduction:

$$O_O^x \rightarrow V_O^{\bullet\bullet} + 2e' + \tfrac{1}{2}O_2 \qquad \text{equation 2}$$

In reducing atmosphere, electronic conductivity takes place via a hopping mechanism and the material behaves as a mixed ionic-electronic conductor. For instance, the ionic transference number of $Ce_{0.8}Gd_{0.2}O_{2-\delta}$ (CGO) at 700 ºC and 10^{-19} atm is as small as 0.5.[60]

Despite the relatively low electronic conductivity of CGO ~0.1 Scm^{-1} at 850 ºC and 10^{-18} atm, recent reports highlighted the very promising properties of acceptor doped ceria as an anode material. As shown by Zhang et al.[61] and by Chueh et al.[62], ceria is able to catalyze the electrochemical oxidation of hydrogen without any metal mediated reaction path; i.e., the whole ceria surface is active. Such a property makes the material extremely interesting for thin film applications. In addition, the sluggish electrical conductivity is mitigated in thin film form owing to the very favorable geometrical factor for out-of-plane conduction (the current collection area / conduction path length ratio is typically in the order of $\approx 10^5$).

Jung et al.[63] demonstrated an unprecedented interfacial anodic reaction resistance value of ≈ 0.2 Ω cm^2 at 650 ºC for porous CGO films of 4.4 μm. The electrochemical activity of the structure was further enhanced by the incorporation low precious metal loadings by sputtering[64] and found practical application in the first example of full-ceramic micro-SOFC based on a

free-standing membrane integrated in Si (figure 8).[59] Interestingly, previous to these works, Fan et al.[65] highlighted the increased performance of a 15 nm, ALD grown, Y-doped CeO_2/sputtered Pt bilayer with respect to a single Pt layer for use as a SOFC thin film anode.

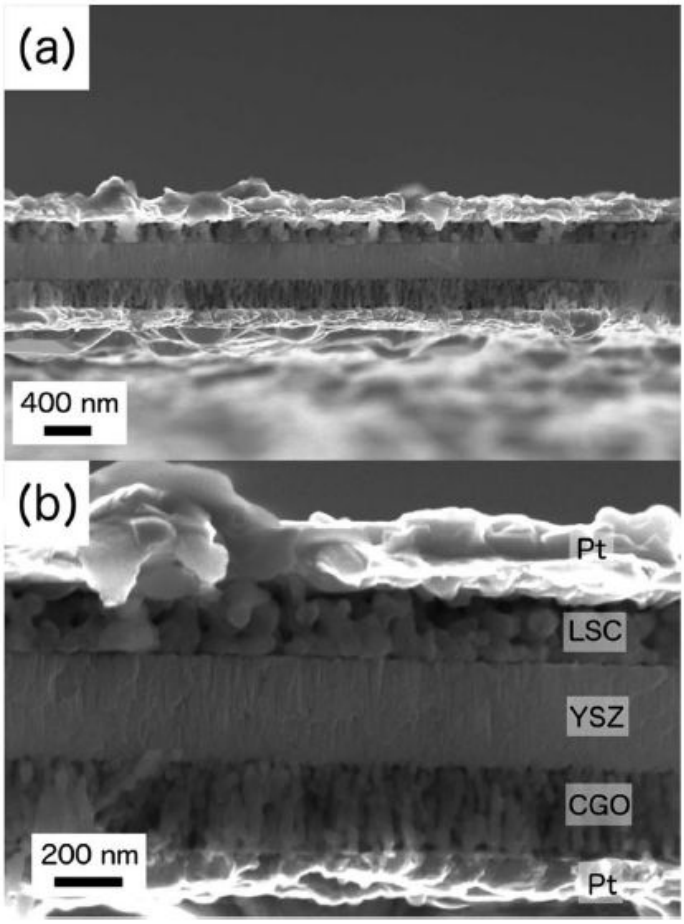

Figure 8. Different magnification cross-sectional SEM images of a full-ceramic microSOFC with YSZ electrolyte and LSCF (cathode) / CGO (anode) electrodes. Reproduced with permission from ref.[59] Copyright 2014, Royal Society of Chemistry.

Although the use of ceria-based thin film anodes has been successfully tested, drawbacks are present especially in relation to the low electronic conductivity which adds up to the SOFC' electrical losses by impeding an efficient current collection. This becomes even more critical in

the case of the porous structures which have been typically employed so far, where current percolation is even poorer. For these reasons, the exploration of new materials with improved electronic conductivity is necessary.

2.2. Acceptor-Doped $SrTiO_3$ and $LaCrO_3$

$SrTiO_3$ (STO) has received interest as a valid alternative anode material owing to an excellent redox stability over a wide range of pO_2, to a very high sulphur resistance and to a good mixed conductivity in reducing conditions for donor doped materials (~1-20 S cm^{-1} at 850 ºC and at 10^{-18} atm).[66,67] Electronic conductivity is obtained by A- or B-site substitution with a higher oxidation state cation, such as La^{3+} or Nb^{5+} for the A- or B-sites, respectively. Charge compensation occurs via the formation of A-site vacancies at high pO_2 or electrons in the low pO_2 regime.

Several works have shown donor-doped STO as an anode material, especially as a backbone component in composites together with materials showing higher catalytic activity.[66,68–70] Nonetheless, fundamental studies on thin film materials and interfaces are rather scarce and examples of its use for portable power devices are missing. This may be ascribed to the strong dependence of the material properties on the A/B cationic ratio, a parameter which becomes of difficult control in physical deposition processes where B-site deficiency is commonly experienced.[71–73] In the case of donor doped $SrTiO_3$, A-site deficiency is necessary in order to limit the formation of Sr-rich secondary phases and extended defects (stemming from Sr^{2+} surface segregation treated previously) that generally affect the final functional properties dramatically.[74] Besides, the sluggish oxidation kinetics of the material may lead to a wide scatter of conductivity values.[75,76] Therefore, the realization of a single-phase, non-stoichiometric, electron compensated donor doped $SrTiO_3$ as thin film anode layer remains an open challenge.

A similar scenario is encountered with respect to another highly promising perovskite compound, namely (La,Sr)(Cr,*M*)O_3 (*M*=Fe, Mn).[54,77] The material features high stability under reducing conditions and a mixed ionic-electronic conducting character upon acceptor doping. The pivotal work of Tao and Irvine[78] highlighted the exceptional stability and high catalytic activity of $La_{1-x}Sr_xCr_{1-y}Mn_yO_3$ (x =0.2-0.3, y ≤0.5 - LSCM), which paved the way towards its technological implementation as a SOFC anode. Here, an anodic polarization resistance of 0.59 Ω cm^2 at 850° C was reported. While the use of the pure LSCM seems advantageous in the case of low-steam hydrocarbons where YSZ-Ni compounds show their main drawback[77], the limiting factor for LSCM is given by the low electronic conduction. Below 10^{-12}-10^{-16} atm and at temperatures between 800 ºC and 1000 ºC, LSCM undergoes a drastic reduction of the p-type conductivity down to 1-3 S cm^{-1}, which is about an order of magnitude less than the expected conductivity for donor-doped STO.[79] Lastly, it should be noted that, to the authors' knowledge, there are no reports on the successful fabrication of LSCM via thin film physical methods. Also the fabrication of the single phase parent compound $La_{1-x}Sr_xCrO_3$ has shown to be difficult to achieve in thin film form.[80,81] This challenges the implementation of Cr-based materials in micro-SOFC.

3. Strategies to Improve Transport and Catalytic Activity of MIEC oxides

3.1. Ex-Solution

Ex-solution of metal nanoparticles and electrochemical switching are remarkable strategies to improve the performance of perovskite-based anodes (figure 9). Recently, these strategies have been reviewed elsewhere.[82] Hence, we provide here some of the key recent advances only. Ex-solution has been widely used in the field of catalysis for a number of years but only recently has recall the attention in the field of materials for SOFC.[5,83,84] Ex-solution consists on the

surface modification of ceramics with an active catalyst (e.g. Ni, Fe, Cu, Ru, Pt) that is incorporated in the lattice as a dopant during the material synthesis. Typically, the dopant is included as a B-site substitutional defect and is ex-solved by exposing the material to reducing conditions. Application of an electric voltage to promote the ex-solution is generally termed electrochemical switching and produces similar results. Both approaches follow the reaction:[84,85]

$$A_{1-\alpha}BO_{3-\delta} \rightarrow (1-\alpha)ABO_{3-\delta'} + \alpha B \qquad \text{equation 3}$$

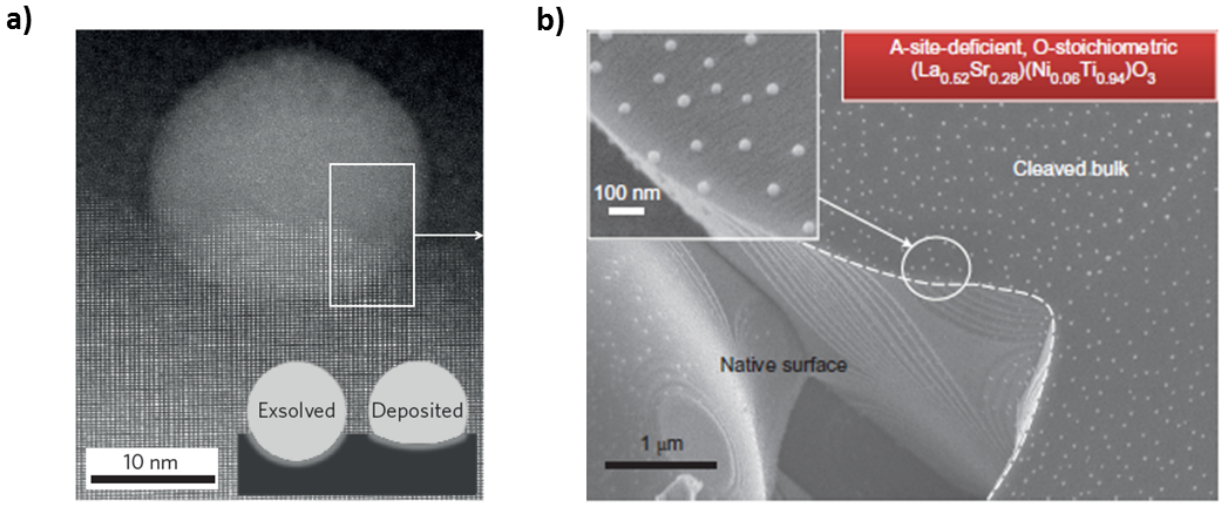

Figure 9. a) TEM image showing ex-solved particles partly immersed in the parent host lattice. b) Perovskite surface after ex-solution: comparison between A-site deficient surface ("cleaved bulk") and stoichiometric surface ("native"). Reproduced with permission from ref.[86,87] Copyright 2013, Nature Publishing Group.

This strategy produces finely dispersed, strongly supported nanoclusters of ~10-50 nm of active metals at the surface of ceramics. A great variety of compositions - mostly perovskite based but, most recently, also fluorite based[88,89] - have been explored.

Most of the works to date on this area have demonstrated a strong enhancement of the materials performance as anode. Goetsch et al.[90] carried out a structural analysis on the appearance of Fe nanoparticles on the surface of thin films, namely on $La_{0.6}Sr_{0.4}FeO_3$, after high temperature annealing, observing a relation between the film phase (orthorhombic or cubic fluorite) and the ability to obtain ex-solution.

Notably, ex-solution has been lately tested also for cathode materials. Chen et al.[91] compared the performance of $PrNi_{0.5}Mn_{0.5}O_3$ (PNMO) surface coated LSCF and untreated LSCF. At 750 °C, the hybrid catalyst-coated LSCF cathode shows a polarization resistance of ~0.022 Ω cm^2, about 6-times lower than that of the uncoated LSCF cathode. They attributed the performance improvement to the presence of highly active PrO_x nanoparticles at the surface ex-solved from the PNMO phase. They propose that these particles represent a preferential site for ORR reaction owing to an easier electron transfer and larger concentration of surface oxygen vacancies. Although the work is mainly focused on particle analysis and on layers obtained by suspension coating, the authors suggested a strategy for the fabrication of an heterostructure also in thin film form by PLD starting from a LSCF/PMNO bilayer. Further investigation on the possibility of obtaining particle decoration via decomposition of a surface layers seems a viable approach for thin films. Yang et al.[92] developed cobalt-free $SrFe_{0.85}Ti_{0.1}Ni_{0.05}O_3$ decorated with NiO nanoparticles obtained by ex-solution. The ORR activity of this material system was larger than state-of-the-art BSCF. The reported electrode ASR, as measured in symmetrical cells at 600 ºC in air atmosphere, was as low as 0.07 Ω cm^2.

The application of ex-solution to thin film materials does not seem to be trivial as only few examples can be found in literature. Limitations related to stoichiometric control (the starting compound should be A-site and oxygen deficient to promote ex-solution) or surface, and

grain-boundary segregation of dopant during the growth process should be overcome to develop this strategy in thin films.

3.2. Grain Boundaries and Space-Charge Effects on Transport and Catalytic Activity

The general structure of a grain boundary in perovskite and fluorite structures has been largely investigated.[93] The crystallographic discontinuity and related lattice distortions which are present at the interface core determine to a great extent the local material chemistry and favor the segregation of cationic and anionic defects.[94] This inherently causes the build-up of an electrical potential (space-charge potential) which modifies the concentration profile of all the mobile species within a nanometer region (space-charge region) across the interface. The space-charge width typically varies from tens of nanometers in case of undoped materials to ~1-2 nm for highly doped materials.[95] As highlighted by experiments on most fluorite and perovskites[94,96], the interface core is typically an area of very low ionic mobility and features positive electric charge (oxygen vacancy excess). In contrast, the space charge zone around the core is generally characterized by negative charge; i.e., it is a depletion zone for oxygen vacancies while electron concentration is enhanced.

The electrochemical considerations described for grain boundaries can also be used for line defects such as dislocations. In dislocations, theoretical and experimental works highlighted the trend for oxygen vacancies to segregate at the defect core[97–99], determining the formation of oxygen-depleted regions in the surrounding space-charge zones.

Space-charge effects have been proven to be an extremely powerful tool for the modification of of the magnitude and type of conductivity of a number of model systems such as ceria[100,101] and STO.[102] However, their effect on oxygen reduction kinetics are limited. For instance, an increase on ORR kinetics was found by Shim et al.[103] in YSZ and by Lee et al.[104] in GDC upon

decrease in grain size. Overall, the limited impact of space-charge effects on the ORR kinetics in many of the classical perovskites can be ascribed to a number of reasons: i) a reduced mobility of oxygen vacancies in the core region, which hinders their participation in the oxygen exchange; ii) the significant oxygen vacancy bulk concentration of typical perovskites (STO, LSC_{113}, LSF), which makes the relative contribution of the grain boundaries to the overall reaction rate negligible; iii) the limited extension of the space-charge region for highly doped systems.

Despite the inherent limitations described, recent reports highlighted that more complex phenomena might come into play and enhanced the ORR kinetics in materials with engineered grain boundaries. Independent works showed a remarkable enhancement of oxygen exchange and diffusion kinetics at the grain boundaries of (La,Sr)MnO_3 (LSM) with respect to the bulk (~3-6 orders of magnitude) as measured by complementary tracer diffusion and EIS.[105,106] This phenomenon has been been the focus of a number of studies in the last years, as it represents a very significant example of grain boundary engineering for SOFC cathodes and may open a new avenue for the fabrication of novel materials.[107,108] Particularly, Chiabrera et al.[108] observed by high resolution transmission electron microscopy (HR-TEM) a high concentration of ordered dislocations and concomitant large enhancement of oxygen vacancies at grain boundaries of manganites. This has been ascribed not just to the well-known reducing nature of dislocation cores, but also to a complex charge compensation mechanism which involves also the presence of B-site vacancies in the bulk. A number of interesting conclusions have been drawn (figure 10a) : i) the introduction of a high concentration of grain boundaries is able to profoundly modify the ORR and oxygen diffusion rates for LSM by enhancing the overall oxygen vacancy content; ii) the oxygen content (and related functional properties) at the interface can be tuned by modifying the A/B ratio in the bulk (this was achieved by combinatorial PLD deposition); iii)

vacancy depletion stemming from space-charge effects is negligible; iv) dislocation cores exhibit high oxygen mobility, thus being able to actively contribute in ORR and oxygen diffusion. Very interestingly, iii) and iv) have been confirmed by a recent computational study by Polfus et al.[109] In their study (figure 10b), they predict that the migration enthalpy for oxygen vacancies along LSM boundaries is as low as 0.5 eV. Whether the appropriate tuning of the grain boundary oxygen concentration and of the bulk stoichiometry can become an universal strategy for ORR engineering is a new and open challenge in the field.[110]

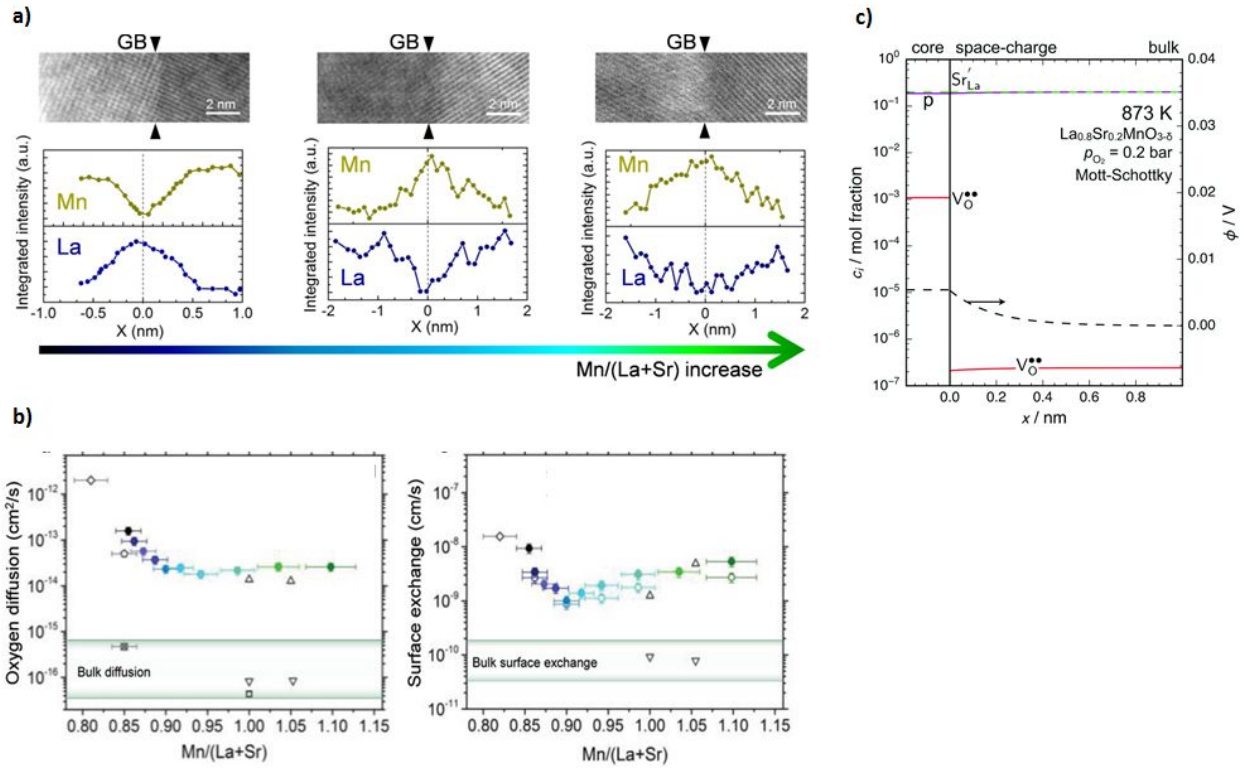

Figure 10. a) Variation of local cation concentration at LSM GBs, retrieved by HR-TEM, as a consequence of a different global A/B ratio after in a LSM library fabricated by combinatorial PLD. b) Oxygen diffusivity and surface exchange coefficient for LSM as a function of the global A/B ratio. a) and b) are reproduced with permission from ref.[108] c) Predicted hole (p), Sr (Sr'_{La}) and oxygen vacancy ($V_O^{\bullet\bullet}$) concentration profile around a dislocation of LSM, together with

space-charge potential profile ø. Reproduced with permission from ref. [109] Copyright 2018, Wiley.

Beside such effect on the chemical environment of bulk materials, some works used the film microstructure to alter the surface chemistry/structure for optimizing ORR kinetics. Januschewsky et al.[111] showed that the decrease of LSC_{113} film crystallinity, occurring when the deposition temperature is lowered, is accompanied by a strong increase of the electrochemical oxygen exchange rate (polarization resistance of 0.1 Ω cm^2 at 600 ºC) and by improved long-term stability. This was arguably related to different segregation of reconstruction behavior of the surface on amorphous and crystalline films. Similar findings were also shown by Develos-Bagarinao et al.[112] on LSCF. They reported fast oxygen diffusion for LSCF with a nanograined structure with a $k^* \sim 10^{-7}$ cm s^{-1} at 600 °C which is about on order of magnitude higher than the reference bulk LSCF. Interestingly, in both LSC_{113} and LSCF one would not expect a major role of grain boundary oxygen vacancies for ORR, since the bulk materials already contains a large oxygen hypostoichiometry. These findings suggest that low crystalline materials seem to be able to stabilize surface structures with enhanced activities, arguably by facilitating charge transfer phenomena. Similar findings have been reported by Chen et al.[22] on Fe-doped STO. In this work, complementary measurements suggested that rapid ORR kinetics is obtained as a trade-off between good crystalline quality (high temperature deposition) and low Sr^{2+} surface concentration. The latter was obtained for samples grown at low temperature and with larger grain boundary density.

4. State-of-the-Art Strategies to Tune Surfaces and Heterointerfaces

4.1. Strain Engineering

The energy landscape of surface reactions can be altered by elastic strain. This becomes particularly important in thin films, where compressive or tensile strain states can be introduced by a number of factors such as i) the presence of heterointerfaces in epitaxial superlattice and VAN thin films; ii) grain boundary formation typically leading to tensile strain; iii) particle impingement during PLD deposition typically leading to compressive strain; iv) or by presence of extended defects.[96] Theoretical and experimental investigations carried out on perovskite cathodes materials, showed that tensile strain is able to accelerate the ORR kinetics. This is a result of an increased vacancy supply (concentration and mobility) and of modification of the surface electronic structure.[113] For example Kushima et al.[114] calculated that elastic tensile strain is able to alter the bulk and surface Co-O bonds in $LaCoO_3$. This decreases the oxygen vacancy formation enthalpy. Cai et al.[115] experimentally confirmed a higher concentration of reduced Co on the surface of tensile stressed LSC_{113} owing to a higher concentration of surface vacancies. Direct measurements on improved ORR kinetics by tensile strain have been carried out by Tsvetkov et al.[116] on Ruddlesen-Popper Nd_2NiO_4 using EIS, by Kubicek et al.[117] on LSC_{113} using tracer diffusion experiments, and by Lee et al.[118] on LSC_{113} using EIS.

It is also worth to notice that recent reports showed that lattice strain is also able to modify the surface chemistry by altering the cationic segregation mechanisms. Koo et al.[119] demonstrated that introducing a large-sized isovalent dopant in Fe-doped STO led to tensile strain and concomitant reduction of Sr^{2+} surface segregation. This resulted in enhanced ORR kinetics. Harrington et al.[120] provided a comprehensive overview of the thermodynamics and kinetics effects of strain on Gd segregation in CGO. Using low energy ion scattering (LEIS), they found an increase in the Gd surface content of tensile strained films as compared to the compressive strained films. However, as highlighted by the authors, kinetics factors might also come into play. Very recently, Han et al.[121] demonstrated that lattice strain can also be used to tune the

exsolution process. They found that a compressive strain increased substantially the density of Ni exsolved nanoparticles in $La_{0.2}Sr_{0.7}Ni_{0.1}Ti_{0.9}O_{3-\delta}$ and was also a successful strategy to reduce the temperature of the reduction process required for the exsolution.

4.2. Photoactivation of Oxygen Reduction Kinetics

The intriguing effects of light on ORR activity have attracted increasing interest in recent times. Merkle et al.[122] first reported a hundred-fold enhancement of the oxygen exchange kinetics upon UV illumination in an “electron poor” material, namely lightly acceptor-doped STO. They suggested that light introduces a surface non-equilibrium state by increasing the electron concentration at the materials surface. This also represented a demonstration of the prominent role that minority carrier concentration can have in ORR kinetics. Such a concept was further expanded also by Jung et al.[17] in $SrTi_xFe_{1-x}O_3$ ($0.05 < x < 1$). They highlighted a strong correlation between surface exchange coefficient and Fermi level position. Hence, they re-affirm the importance of the minority electron carrier density but, in this case, in heavily doped materials. Kim et al.[123] showed recently that illumination is not only able to affect the electronic concentration, but also the ionic concentration. Here, it has been shown that light can increase by orders of magnitude the ionic conductivity of methylammonium lead iodide. Such a discovery may open up an interesting scenario for tailoring ORR kinetics owing to tunable light-induced oxygen vacancy concentration. Indeed, the concept of “band engineering” by properly tailored interfaces[45] together with external perturbations such as light or also electric field[124] opens an avenue to tune surface states and search for novel functionalities.

Recently, the concept of photoactivation has also been applied to fabricate devices. Walch et al.[125] reported a “solid oxide photoelectrochemical cell” consisting of a zirconia-based electrochemical cell with single crystalline STO electrodes. Once the STO surface is illuminated at high temperature, the device featured a build-up of a battery-type voltage up to 300 mV. The

voltage build-up was attributed to a faster incorporation kinetics at the “excited” STO surface, leading to an oxygen potential gradient in the material.

Conclusions

Recent years have seen a remarkable improvement in the catalytic and transport properties of mixed ionic electronic conducting oxides. These materials are critical for solid oxide fuel cells, membranes, sensors, among many other devices. Most of these improvements stem from the development of controlled nanostructures. At surfaces, decoration with low content of noble metals and oxides of dissimilar crystal structure from the host matrix have advanced the field substantially. The latter provides a much more relevant strategy for technological implementation owing to reduced costs and long-term reliability. Atomic layer deposition, surface treatments with aqueous solutions or controlled segregation of surface species in operando (ex-solution or electrochemical switching) have provided some of the most promising recent results of surface engineering to enhanced the catalytic activity of oxides for both oxidation and reduction reactions.

The development of engineered grain boundaries in fluorites and perovskites also provides a concise strategy to improve further transport properties and it may also open the opportunity of improving oxygen exchange kinetics. Nonetheless, tuning grain boundaries to improve catalytic properties remains largely unexplored. The development of heterointerfaces between perovskites and Ruddlesden-Popper phases has been consolidated recently as a remarkable strategy to enhance both transport properties and oxygen exchange kinetics. The exact mechanism(s) governing the heterointerface functionality are still questioned and certainly warrant further investigation. Vertically aligned nanocomposites will be quite useful to probe engineered heterointerfaces to understand fundamental mechanisms and to exploit them in

devices. We also anticipate that strain engineering and photoactivation of surfaces and interfaces can render new functionalities. This offers a remarkable yet barely explored opportunity to tune transport and catalytic properties. We would also like to stress the importance of detailed experimental procedures, careful realization of experiments to facilitate reproducibility, and in-depth analysis of the electrochemical mechanisms governing the materials' functionality. These notions are of paramount importance to keep on advancing the exciting field of mixed ionic electronic materials for electrochemical energy devices.

Acknowledgements

M. A. acknowledges the support of the Feodor Lynen Research Fellowship Program of the Alexander von Humboldt Foundation as well as the contribution of the Isaac Newton Trust. M. A. and J. L. M.-D. acknowledge the support of the Center for Advanced Materials for Integrated Energy Systems under EP/P007767/1 and ERC-POC grant 779444, Portapower. Part of this work has been funded by the European Union's Horizon 2020 research and innovation programme under grant agreement No 824072 (Harvestore) and by COST Action – STMS (MP1308).

References

[1] I. Staffell, D. Scamman, A. Velazquez Abad, P. Balcombe, P. E. Dodds, P. Ekins, N. Shah, K. R. Ward, *Energy & Environmental Science* **2019**, *12*, 463.
[2] W. H. Kan, A. J. Samson, V. Thangadurai, *J. Mater. Chem. A* **2016**, *4*, 17913.
[3] Y. Zhang, R. Knibbe, J. Sunarso, Y. Zhong, W. Zhou, Z. Shao, Z. Zhu, *Advanced Materials* **2017**, *29*, 1700132.
[4] W. Deibert, M. E. Ivanova, S. Baumann, O. Guillon, W. A. Meulenberg, *Journal of Membrane Science* **2017**, *543*, 79.
[5] P. Boldrin, E. Ruiz-Trejo, J. Mermelstein, J. M. Bermúdez Menéndez, T. Ramírez Reina, N. P. Brandon, *Chemical Reviews* **2016**, *116*, 13633.
[6] Y. Zhang, R. Knibbe, J. Sunarso, Y. Zhong, W. Zhou, Z. Shao, Z. Zhu, *Advanced Materials* **2017**, *29*, 1700132.
[7] Y. Chen, W. Zhou, D. Ding, M. Liu, F. Ciucci, M. Tade, Z. Shao, *Advanced Energy Materials* **2015**, *5*, 1500537.

[8] P. A. Connor, X. Yue, C. D. Savaniu, R. Price, G. Triantafyllou, M. Cassidy, G. Kerherve, D. J. Payne, R. C. Maher, L. F. Cohen, R. I. Tomov, B. A. Glowacki, R. V. Kumar, J. T. S. Irvine, *Advanced Energy Materials* **2018**, *8*, 1.
[9] X. Xu, W. Wang, W. Zhou, Z. Shao, *Small Methods* **2018**, *2*, 1800071.
[10] B. Koo, K. Kim, J. K. Kim, H. Kwon, J. W. Han, W. Jung, *Joule* **2018**, *2*, 1476.
[11] Z. Feng, W. T. Hong, D. D. Fong, Y.-L. Lee, Y. Yacoby, D. Morgan, Y. Shao-Horn, *Accounts of Chemical Research* **2016**, *49*, 966.
[12] X.-K. Gu, S. Samira, E. Nikolla, *Chemistry of Materials* **2018**, *30*, 2860.
[13] L. Wang, R. Merkle, Y. A. Mastrikov, E. A. Kotomin, J. Maier, *Journal of Materials Research* **2012**, *27*, 2000.
[14] R. A. De Souza, *Physical Chemistry Chemical Physics* **2006**, *8*, 890.
[15] R. A. De Souza, J. A. Kilner, *Solid State Ionics* **1999**, 9.
[16] A. Infortuna, A. S. Harvey, L. J. Gauckler, *Advanced Functional Materials* **2008**, *18*, 127.
[17] W. Jung, H. L. Tuller, *Advanced Energy Materials* **2011**, *1*, 1184.
[18] M. Riva, M. Kubicek, X. Hao, G. Franceschi, S. Gerhold, M. Schmid, H. Hutter, J. Fleig, C. Franchini, B. Yildiz, U. Diebold, *Nature Communications* **2018**, *9*, DOI 10.1038/s41467-018-05685-5.
[19] N. Tsvetkov, Q. Lu, L. Sun, E. J. Crumlin, B. Yildiz, *Nature Materials* **2016**, *15*, 1010.
[20] G. M. Rupp, A. K. Opitz, A. Nenning, A. Limbeck, J. Fleig, *Nature Materials* **2017**, *16*, 640.
[21] Y. Chen, A. Hinerman, L. Liang, K. Gerdes, S. P. Navia, J. Prucz, X. Song, *Journal of Power Sources* **2018**, *405*, 45.
[22] T. Chen, G. F. Harrington, K. Sasaki, N. H. Perry, *Journal of Materials Chemistry A* **2017**, *5*, 23006.
[23] A. Evans, J. Martynczuk, D. Stender, C. W. Schneider, T. Lippert, M. Prestat, *Advanced Energy Materials* **2015**, *5*, 1400747.
[24] Y. Chen, Y. Choi, S. Yoo, Y. Ding, R. Yan, K. Pei, C. Qu, L. Zhang, I. Chang, B. Zhao, Y. Zhang, H. Chen, Y. Chen, C. Yang, B. deGlee, R. Murphy, J. Liu, M. Liu, *Joule* **2018**, *2*, 938.
[25] Y. Wen, T. Yang, D. Lee, H. N. Lee, E. J. Crumlin, K. Huang, *Journal of Materials Chemistry A* **2018**, *6*, 24378.
[26] Y. Li, W. Zhang, T. Wu, Y. Zheng, J. Chen, B. Yu, J. Zhu, M. Liu, *Advanced Energy Materials* **2018**, 1801893.
[27] E. J. Crumlin, E. Mutoro, S.-J. Ahn, G. J. la O', D. N. Leonard, A. Borisevich, M. D. Biegalski, H. M. Christen, Y. Shao-Horn, *The Journal of Physical Chemistry Letters* **2010**, *1*, 3149.
[28] T. Hong, M. Zhao, K. Brinkman, F. Chen, C. Xia, *ACS Applied Materials & Interfaces* **2017**, *9*, 8659.
[29] S. Lee, J. L. MacManus-Driscoll, *APL Materials* **2017**, *5*, 042304.
[30] J. L. MacManus-Driscoll, A. Suwardi, H. Wang, *MRS Bulletin* **2015**, *40*, 933.
[31] A. Chen, Q. Su, H. Han, E. Enriquez, Q. Jia, *Advanced Materials* **2019**, *31*, 1803241.
[32] L. dos Santos Gómez, S. Sanna, P. Norby, N. Pryds, D. Marrero-López, E. R. Losilla, V. Esposito, *Nanoscale* **2019**.
[33] Y.-W. Ju, J. Hyodo, A. Inoishi, S. Ida, T. Tohei, Y.-G. So, Y. Ikuhara, T. Ishihara, *Advanced Energy Materials* **2014**, *4*, 1400783.
[34] J. Yoon, S. Cho, J.-H. Kim, J. Lee, Z. Bi, A. Serquis, X. Zhang, A. Manthiram, H. Wang, *Advanced Functional Materials* **2009**, *19*, 3868.
[35] M. Sase, *Solid State Ionics* **2008**, *178*, 1843.
[36] M. Sase, F. Hermes, K. Yashiro, K. Sato, J. Mizusaki, T. Kawada, N. Sakai, H. Yokokawa,

Journal of The Electrochemical Society **2008**, *155*, B793.
[37] M. Sase, F. Hermes, T. Nakamura, K. Yashiro, K. Sato, J. Mizusaki, T. Kawada, N. Sakai, K. Yamaji, T. Horita, H. Yokokawa, *ECS Trans.* **2007**, *7*, 1055.
[38] Y. Zheng, Y. Li, T. Wu, W. Zhang, J. Zhu, Z. Li, J. Chen, B. Yu, J. Wang, J. Zhang, *Nano Energy* **2018**, *51*, 711.
[39] S. Stämmler, R. Merkle, J. Maier, *Journal of The Electrochemical Society* **2017**, *164*, F454.
[40] S. Stämmler, R. Merkle, B. Stuhlhofer, G. Logvenov, K. Hahn, P. A. van Aken, J. Maier, *Solid State Ionics* **2017**, *303*, 172.
[41] S. Stammler, R. Merkle, B. Stuhlhofer, G. Logvenov, J. Maier, *ECS Transactions* **2015**, *68*, 579.
[42] W. Ma, J. J. Kim, N. Tsvetkov, T. Daio, Y. Kuru, Z. Cai, Y. Chen, K. Sasaki, H. L. Tuller, B. Yildiz, *J. Mater. Chem. A* **2015**, *3*, 207.
[43] D. Sari, F. Piskin, Z. C. Torunoglu, B. Yasar, Y. E. Kalay, T. Ozturk, *Solid State Ionics* **2018**, *326*, 124.
[44] N. Tsvetkov, Y. Chen, B. Yildiz, *Journal of Materials Chemistry A* **2014**, *2*, 14690.
[45] Y. Chen, D. D. Fong, F. W. Herbert, J. Rault, J.-P. Rueff, N. Tsvetkov, B. Yildiz, *Chemistry of Materials* **2018**, *30*, 3359.
[46] C. Zhao, X. Liu, W. Zhang, Y. Zheng, Y. Li, B. Yu, J. Wang, J. Chen, *International Journal of Hydrogen Energy* **2018**, DOI 10.1016/j.ijhydene.2018.04.128.
[47] Z. Feng, Y. Yacoby, M. J. Gadre, Y.-L. Lee, W. T. Hong, H. Zhou, M. D. Biegalski, H. M. Christen, S. B. Adler, D. Morgan, Y. Shao-Horn, *The Journal of Physical Chemistry Letters* **2014**, *5*, 1027.
[48] M. J. Gadre, Y.-L. Lee, D. Morgan, *Physical Chemistry Chemical Physics* **2012**, *14*, 2606.
[49] D. Lee, Y.-L. Lee, W. T. Hong, M. D. Biegalski, D. Morgan, Y. Shao-Horn, *Journal of Materials Chemistry A* **2015**, *3*, 2144.
[50] Y.-L. Lee, J. Kleis, J. Rossmeisl, Y. Shao-Horn, D. Morgan, *Energy & Environmental Science* **2011**, *4*, 3966.
[51] B. Koo, K. Kim, J. K. Kim, H. Kwon, J. W. Han, W. Jung, *Joule* **2018**, *2*, 1476.
[52] C. Lenser, Q. Lu, E. Crumlin, H. Bluhm, B. Yildiz, *The Journal of Physical Chemistry C* **2018**, *122*, 4841.
[53] K. Develos-Bagarinao, J. De Vero, H. Kishimoto, T. Ishiyama, K. Yamaji, T. Horita, H. Yokokawa, *Nano Energy* **2018**, *52*, 369.
[54] E. V. Tsipis, V. V. Kharton, *Journal of Solid State Electrochemistry* **2008**, *12*, 1367.
[55] M. Radovic, S. A. Speakman, L. F. Allard, E. A. Payzant, E. Lara-Curzio, W. M. Kriven, J. Lloyd, L. Fegely, N. Orlovskaya, *Journal of Power Sources* **2008**, *184*, 77.
[56] T. Setoguchi, K. Okamoto, K. Eguchi, H. Arai, *Journal of The Electrochemical Society* **1992**, *139*, 2875.
[57] S. Zha, Z. Cheng, M. Liu, *Journal of The Electrochemical Society* **2007**, *154*, B201.
[58] F. J. Garcia-Garcia, F. Yubero, A. R. Gonz Alez-Elipe, S. P. Balomenou, D. Tsiplakides, I. Petrakopoulou, R. M. Lambert, *International Journal of Hydrogen Energy* **2015**, *40*, 7382.
[59] I. Garbayo, D. Pla, A. Morata, L. Fonseca, N. Sabaté, A. Tarancón, *Energy Environ. Sci.* **2014**, *7*, 3617.
[60] T. Kudo, H. Obayashi, *J. Electrochem. Soc.* **1975**, *122*, 142.
[61] C. Zhang, M. E. Grass, A. H. McDaniel, S. C. DeCaluwe, F. E. Gabaly, Z. Liu, K. F. McCarty, R. L. Farrow, M. A. Linne, Z. Hussain, G. S. Jackson, H. Bluhm, B. W. Eichhorn, *Nature Materials* **2010**, *9*, 944.
[62] W. C. Chueh, S. M. Haile, *Physical Chemistry Chemical Physics* **2009**, *11*, 8144.
[63] W. Jung, J. O. Dereux, W. C. Chueh, Y. Hao, S. M. Haile, **n.d.**, DOI 10.1039/c2ee22151a.

[64] W. Jung, K. L. Gu, Y. Choi, S. M. Haile, *Energy Environ. Sci.* **2014**, *7*, 1685.
[65] Z. Fan, F. B. Prinz, *Nano Letters* **2011**, DOI 10.1021/nl104417n.
[66] T. S. Oh, A. S. Yu, L. Adijanto, R. J. Gorte, J. M. Vohs, *Journal of Power Sources* **2014**, *262*, 207.
[67] T. Shi, Y. Chen, X. Guo, *Progress in Materials Science* **2016**, *80*, 77.
[68] D. Burnat, G. Nurk, L. Holzer, M. Kopecki, A. Heel, *Journal of Power Sources* **2018**, *385*, 62.
[69] P. Blennow, K. K. Hansen, L. R. Wallenberg, M. Mogensen, *Solid State Ionics* **2009**, *180*, 63.
[70] X. Shen, K. Sasaki, *Journal of Power Sources* **2016**, *320*, 180.
[71] D. J. Keeble, R. A. MacKie, W. Egger, B. Löwe, P. Pikart, C. Hugenschmidt, T. J. Jackson, *Physical Review B - Condensed Matter and Materials Physics* **2010**, DOI 10.1103/PhysRevB.81.064102.
[72] P. Blennow, K. K. Hansen, L. R. Wallenberg, M. Mogensen, *Electrochimica Acta* **2006**, *52*, 1651.
[73] J. Chen, M. Döbeli, D. Stender, K. Conder, A. Wokaun, C. W. Schneider, T. Lippert, *Applied Physics Letters* **2014**, DOI 10.1063/1.4895788.
[74] P. R. Slater, D. P. Fagg, J. T. S. Irvine, *Journal of Materials Chemistry* **1997**, DOI 10.1039/a702865b.
[75] J. W. Fergus, *Solid State Ionics* **2006**, *177*, 1529.
[76] O. A. Marina, N. L. Canfield, J. W. Stevenson, *Solid State Ionics* **2002**, *149*, 21.
[77] S. Tao, J. T. S. Irvine, *Journal of The Electrochemical Society* **2004**, *151*, A252.
[78] S. Tao, J. T. S. Irvine, *Nature Materials* **2003**, *2*, 320.
[79] V. V. Kharton, V. E. Tsipis, I. P. Marozau, A. P. Viskup, J. R. Frade, J. T. S. Irvine, *Solid State Ionics* **2007**, *178*, 101.
[80] A. Kajimura, H. Sasaki, S. Otoshi, M. Suzuki, M. Ippommatsu, T. Kawai, S. Kawai, *Preparation of La1-x SrxCr03 by Film by Laser Ablation Method*, **1995**.
[81] G. C. Brunauer, B. Rotter, G. Walch, E. Esmaeili, A. K. Opitz, K. Ponweiser, J. Summhammer, J. Fleig, *Advanced Functional Materials* **2016**, *26*, 120.
[82] K. Huang, *Science Bulletin* **2016**, *61*, 1783.
[83] B. D. Madsen, W. Kobsiriphat, Y. Wang, L. D. Marks, S. A. Barnett, *Journal of Power Sources* **2007**, *166*, 64.
[84] D. Neagu, G. Tsekouras, D. N. Miller, H. Ménard, J. T. S. Irvine, *Nature Chemistry* **2013**, *5*, 916.
[85] J. Myung, D. Neagu, D. N. Miller, J. T. S. Irvine, *Nature* **2016**, *537*, 528.
[86] D. Neagu, G. Tsekouras, D. N. Miller, H. Ménard, J. T. S. Irvine, *Nature Chemistry* **2013**, *5*, 916.
[87] D. Neagu, T.-S. Oh, D. N. Miller, H. Ménard, S. M. Bukhari, S. R. Gamble, R. J. Gorte, J. M. Vohs, J. T. S. Irvine, *Nature Communications* **2015**, *6*, 8120.
[88] S. Gatla, D. Aubert, V. Flaud, R. Grosjean, T. Lunkenbein, O. Mathon, S. Pascarelli, H. Kaper, *Catalysis Today* **2018**, 0.
[89] J. Tan, D. Lee, J. Ahn, B. Kim, J. Kim, J. Moon, *J. Mater. Chem. A* **2018**, *6*, 18133.
[90] T. Götsch, N. Köpfle, M. Grünbacher, J. Bernardi, E. A. Carbonio, M. Hävecker, A. Knop-Gericke, M. F. Bekheet, L. Schlicker, A. Doran, A. Gurlo, A. Franz, B. Klötzer, S. Penner, *Phys. Chem. Chem. Phys.* **2019**, *21*, 3781.
[91] Y. Chen, Y. Chen, D. Ding, Y. Ding, Y. Choi, L. Zhang, S. Yoo, D. Chen, B. deGlee, H. Xu, Q. Lu, B. Zhao, G. Vardar, J. Wang, H. Bluhm, E. J. Crumlin, C. Yang, J. Liu, B. Yildiz, M. Liu, *Energy & Environmental Science* **2017**, *10*, 964.

[92] G. Yang, W. Zhou, M. Liu, Z. Shao, *ACS Applied Materials & Interfaces* **2016**, *8*, 35308.
[93] J. Maier, *Berichte der Bunsengesellschaft für physikalische Chemie* **1986**, *90*, 26.
[94] F. Chiabrera, I. Garbayo, A. Tarancón, in *Metal Oxide-Based Thin Film Structures* (Eds.: N. Pryds, V. Esposito), Elsevier, **2018**, pp. 409–439.
[95] D. S. Mebane, R. A. De Souza, *Energy & Environmental Science* **2015**, *8*, 2935.
[96] I. Garbayo, F. Baiutti, A. Morata, A. Tarancón, *Journal of the European Ceramic Society* **2019**, *39*, 101.
[97] D. Marrocchelli, L. Sun, B. Yildiz, *Journal of the American Chemical Society* **2015**, *137*, 4735.
[98] L. Sun, D. Marrocchelli, B. Yildiz, *Nature Communications* **2015**, *6*, 6294.
[99] V. Metlenko, A. H. H. Ramadan, F. Gunkel, H. Du, H. Schraknepper, S. Hoffmann-Eifert, R. Dittmann, R. Waser, R. A. De Souza, *Nanoscale* **2014**, *6*, 12864.
[100] A. Tschöpe, E. Sommer, R. Birringer, *Solid State Ionics* **2001**, *139*, 255.
[101] M. C. Göbel, G. Gregori, J. Maier, *Solid State Ionics* **2012**, *215*, 45.
[102] P. Lupetin, G. Gregori, J. Maier, *Angewandte Chemie International Edition* **2010**, *49*, 10123.
[103] J. H. Shim, J. S. Park, T. P. Holme, K. Crabb, W. Lee, Y. B. Kim, X. Tian, T. M. Gür, F. B. Prinz, *Acta Materialia* **2012**, *60*, 1.
[104] W. Lee, H. J. Jung, M. H. Lee, Y.-B. Kim, J. S. Park, R. Sinclair, F. B. Prinz, *Advanced Functional Materials* **2012**, *22*, 965.
[105] E. Navickas, T. M. Huber, Y. Chen, W. Hetaba, G. Holzlechner, G. Rupp, M. Stöger-Pollach, G. Friedbacher, H. Hutter, B. Yildiz, J. Fleig, *Physical Chemistry Chemical Physics* **2015**, *17*, 7659.
[106] A. M. Saranya, D. Pla, A. Morata, A. Cavallaro, J. Canales-Vázquez, J. A. Kilner, M. Burriel, A. Tarancón, *Advanced Energy Materials* **2015**, *5*, 1500377.
[107] E. Navickas, Y. Chen, Q. Lu, W. Wallisch, T. M. Huber, J. Bernardi, M. Stöger-Pollach, G. Friedbacher, H. Hutter, B. Yildiz, J. Fleig, *ACS Nano* **2017**, *11*, 11475.
[108] F. Chiabrera, I. Garbayo, L. López-Conesa, G. Martín, A. Ruiz-Caridad, M. Walls, L. Ruiz-González, A. Kordatos, M. Núñez, A. Morata, S. Estradé, A. Chroneos, F. Peiró, A. Tarancón, *Advanced Materials* **2019**, *31*, 1805360.
[109] J. M. Polfus, B. Yildiz, H. L. Tuller, *Physical Chemistry Chemical Physics* **2018**, *20*, 19142.
[110] T. Frömling, S. Steiner, A. Ayrikyan, D. Bremecker, M. Dürrschnabel, L. Molina-Luna, H.-J. Kleebe, H. Hutter, K. G. Webber, M. Acosta, *Journal of Materials Chemistry C* **2017**, DOI 10.1039/C7TC03975A.
[111] J. Januschewsky, M. Ahrens, A. Opitz, F. Kubel, J. Fleig, *Advanced Functional Materials* **2009**, *19*, 3151.
[112] K. Develos-Bagarinao, H. Kishimoto, J. De Vero, K. Yamaji, T. Horita, *Solid State Ionics* **2016**, *288*, 6.
[113] B. Yildiz, *MRS Bulletin* **2014**, *39*, 147.
[114] A. Kushima, S. Yip, B. Yildiz, *Phys. Rev. B* **2010**, *82*, 115435.
[115] Z. Cai, Y. Kuru, J. W. Han, Y. Chen, B. Yildiz, *Journal of the American Chemical Society* **2011**, *133*, 17696.
[116] N. Tsvetkov, Q. Lu, Y. Chen, B. Yildiz, *ACS Nano* **2015**, *9*, 1613.
[117] M. Kubicek, Z. Cai, W. Ma, B. Yildiz, H. Hutter, J. Fleig, *ACS Nano* **2013**, *7*, 3276.
[118] D. Lee, R. Jacobs, Y. Jee, A. Seo, C. Sohn, A. V. Ievlev, O. S. Ovchinnikova, K. Huang, D. Morgan, H. N. Lee, *The Journal of Physical Chemistry C* **2017**, *121*, 25651.
[119] B. Koo, H. Kwon, Y. Kim, H. G. Seo, J. W. Han, W. Jung, *Energy & Environmental Science* **2018**, *11*, 71.

[120] G. F. Harrington, S. J. Skinner, J. A. Kilner, *Journal of the American Ceramic Society* **2018**, *101*, 1310.
[121] H. Han, J. Park, S. Y. Nam, K. J. Kim, G. M. Choi, S. S. P. Parkin, H. M. Jang, J. T. S. Irvine, *Nature Communications* **2019**, *10*, 1471.
[122] R. Merkle, R. A. De Souza, J. Maier, *Angewandte Chemie International Edition* **2001**, *40*, 2126.
[123] G. Y. Kim, A. Senocrate, T.-Y. Yang, G. Gregori, M. Grätzel, J. Maier, *Nature Materials* **2018**, *17*, 445.
[124] B. W. Veal, S. K. Kim, P. Zapol, H. Iddir, P. M. Baldo, J. A. Eastman, *Nature Communications* **2016**, *7*, DOI 10.1038/ncomms11892.
[125] G. Walch, B. Rotter, G. C. Brunauer, E. Esmaeili, A. K. Opitz, M. Kubicek, J. Summhammer, K. Ponweiser, J. Fleig, *Journal of Materials Chemistry A* **2017**, *5*, 1637.